ADVANCED OPTICAL MATERIALS
www.advopticalmat.de

Stabilizing 2D Pt-Based Halide Perovskites via Solvent Lone Pair Donation

*Huilong Liu, Maitreyo Biswas, Walter J. Smith, Edward Barnard, Thomas Beechem, Arun Mannodi-Kanakkithodi, and Shubhra Bansal**

Platinum-based halide perovskites exhibit promising optoelectronic properties along with merits of low-temperature processing and stability. Current research on Pt halide perovskites is limited to 0D A_2BX_6 structure as the ABX_3 3D structure is thermodynamically unstable. Herein, the study reports the stabilization of the ABX_3 structure into a 2D layered phase, $CsPtI_3(DMSO)$, that is stable up to 181.5 °C. The 2D phase shows an excitonic peak at the absorption edge of 600 nm, indicating quantum confinement. It also exhibits a large Stokes shift due to intersystem crossing (ISC), with a quenched singlet excitonic fluorescence at 610 nm and strong triplet emission at 852 nm. Pt(II) co-ordinates with dimethyl sulfoxide (DMSO) via σ-donation of S lone-pair electrons and π- back donation from Pt to S, stabilizing $CsPtI_3(DMSO)$ layered structure. The strong electronic interaction between DMSO and Pt(II) and orbital mixing lead to spin-orbit-coupling, facilitating ISC and singlet-to-triplet exciton energy transfer. The interaction of Pt and DMSO is further confirmed by addition of thioacetamide (TAA), a strong S-donor, which retards the formation of 2D layered structure, and directly results in Cs_2PtI_6 and Pt.

1. Introduction

Attributable to the remarkable optoelectronic properties including tunable and strong broadband light absorption, high extinction coefficient, long carrier lifetime, and defect tolerance, metal halide perovskites (MHPs) have recently attracted extensive attention for solar energy conversion materials.[1–3] Moreover, MHPs are solution processable and compatible with low cost thin-film deposition techniques.[4,5] Pb-based perovskites, (e.g., $CsPbBr_3$, $MAPbI_3$, $FAPbBr_3$) have proven advantages in applications like light emitting diodes (LEDs),[6] photocatalysis,[7,8] detectors,[9] and photovoltaics (PV).[10] However, the non-negligible environmental risks associated with lead toxicity[11–13] and stability issues[10,14] impede their commercial applications.

Reducing crystal structure dimensionality provides a means of enhancing MHP stability while also providing additional pathways to tailor the optoelectronic properties of the material. For example, two-dimensional (2D) Pb- and Sn-halide perovskites have shown promise with improved environmental stability, also exhibiting unique optoelectronic properties due to quantum confinement effects.[15–17] To achieve this dimensional reduction from 3D to 2D, halide perovskites have been modified using bulky organic spacer molecules between inorganic corner- or edge-shared octahedra sheets. Spacer molecules play a significant role in adjusting the properties of the 2D phase, influencing octahedral distortion, M–X–M bond angles, exciton binding energy, and material stability. Additionally, an important aspect of the classification of 2D halide perovskites is the crystallographic plane along which the 3D structure is cleaved such as (100), (110), and (111). Typical 2D perovskite phases include (100)- oriented Ruddlesden-Popper (RP) or Dion-Jacobson (DJ) or alternating cation in the interlayer spacer (ACI) phases. Some exceptions being $Cs_2SnI_2Cl_2$, $Cs_2PbI_2Cl_2$, where the crystal is naturally 2D; and $(MA)_2PbI_2(SCN)_2$ with partial halide substitution by thiocyanate (SCN) separating the 2D layers.[18–20] Despite the promising stability of dimensionally modified (2D, 1D, 0D) MHPs, Pb-toxicity challenge remains, and the research community continues to explore Pb-free alternatives.

Cs_2PtI_6 has emerged as a promising Pb-free halide perovskite due to its merits including: 1) non-toxicity and biocompatibility, 2) tunable bandgap with excellent panchromatic visible light absorption, 3) quasi-direct semiconducting nature beneficial for carrier generation, 4) high carrier mobility and lifetime.[21–37]

H. Liu, W. J. Smith, T. Beechem, S. Bansal
School of Mechanical Engineering
Purdue University
West Lafayette, IN 47907, USA
E-mail: bansal91@purdue.edu

M. Biswas, A. Mannodi-Kanakkithodi, S. Bansal
School of Materials Engineering
Purdue University
West Lafayette, IN 47907, USA

E. Barnard
Molecular Foundry
Lawrence Berkeley National Laboratory
Berkeley, CA 94720, USA

The ORCID identification number(s) for the author(s) of this article can be found under https://doi.org/10.1002/adom.202402435

DOI: 10.1002/adom.202402435

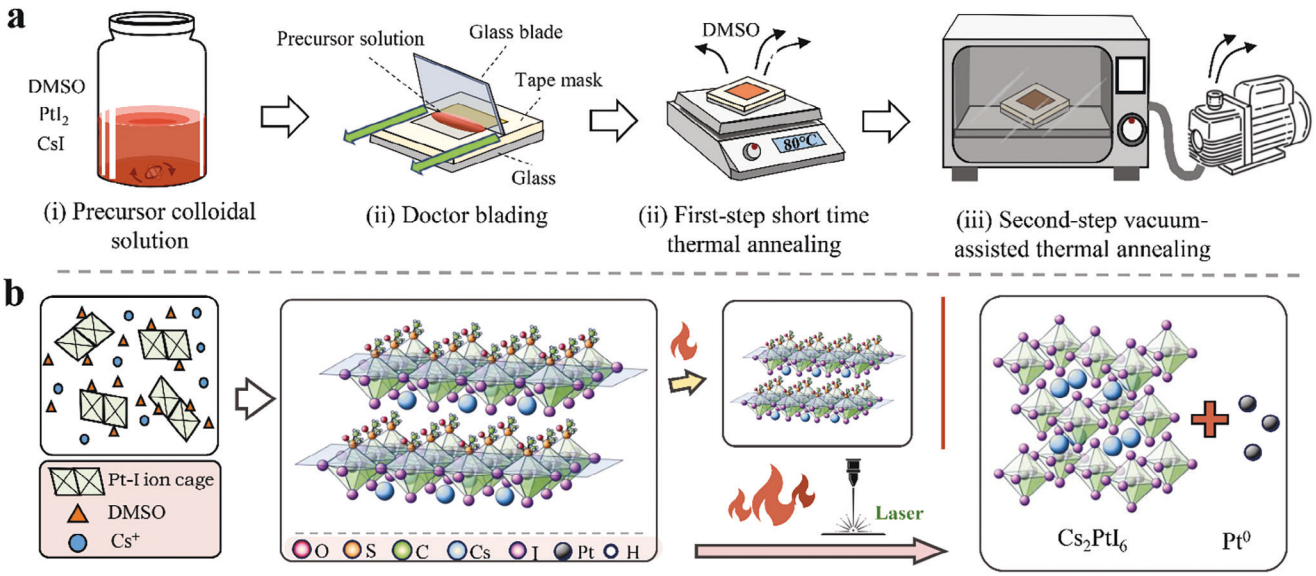

Figure 1. a) Process schematic for doctor blading perovskite thin film with "two-step" annealing. b) The nano-assemble model for crystallization and phase transition from 2D- $CsPtI_3$(DMSO) to 0D- Cs_2PtI_6 perovskite after thermal or laser annealing.

Most notably, the recent demonstration of extraordinary stability in harsh conditions, including decomposition temperature of 350 °C, long-term ambient stability for at least one year, and stability in aqueous solutions of extremely acid and basic pH (1 and 13) for 24 hours; make Cs_2PtI_6 very promising for applications including PV, LEDs, and photocatalysis, etc.[22,23,25] The structural and thermodynamic stability have also been validated by first-principle calculations with Goldschmidt tolerance factor of 0.962, octahedral factor of 0.364, formation energy of −7.44 eV per formula unit and Gibbs free energy for decomposition of −0.77 eV/atom.[28,34,35] Previous work from Schwartz et al.[36] has shown the calculated band structure of Cs_2PtI_6, revealing that the material can exhibit both indirect and direct bandgaps with valence band (VB) derived primarily from *I p* states, and conduction band (CB) derived from hybridized *Pt d* and *I p* states. Recent numerical simulations estimate practical efficiency limit for Cs_2PtI_6 devices of 23.52%,[30] competitive with state-of-the-art 26.1% for organic-inorganic hybrid Pb-halide perovskite solar cells.[38] Given the promising properties of Cs_2PtI_6, it is exciting to explore the structure-property correlations of dimensionally modified Pt-halide perovskites, as a Pb-free alternative.

Herein, for the first time, we report stabilization of $CsPtI_3$ into a layered 2D perovskite via Pt(II) co-ordination with S lone-pair electrons in DMSO, which substitute the iodide in octahedra as bound ligand spacer molecules to separate the 2D layers. DFT calculations (PBEsol+D3) reveal the positive decomposition energy of the cubic phase of 3D $CsPtI_3$, indicating it is thermodynamically unstable. However, the formation of a stable σ-bond between Pt and S lone-pair electrons stabilizes the 2D-$CsPtI_3$(DMSO) with a negative decomposition energy of $\Delta H = -1.69$ eV per formula unit. 2D- $CsPtI_3$(DMSO) perovskite thin-films are fabricated using doctor blade method, which can decompose to Cs_2PtI_6 + Pt at 181.5 °C or laser annealing. The formation and transformation of the 2D phase has been experimentally observed with scanning electron microscopy (SEM), energy dispersive X-ray spectrometry (EDS), X-Ray diffraction analysis (XRD), Fourier transform infrared spectroscopy (FTIR), UV–vis–NIR absorption spectroscopy, thermogravimetric analysis (TGA), Raman and photoluminescence (PL) spectroscopy. Pt(II)-DMSO coordination was further confirmed by addition of Lewis bases such as acetamide (AA), 1,3-Dimethyl-3,4,5,6-tetrahydro-2(1H)-pyrimidinone (DMPU), and thioacetamide (TAA). TAA, which also has S-donor atoms, is the only additive found to impede the formation of 2D- $CsPtI_3$(DMSO) phase, resulting directly in the formation of Cs_2PtI_6. For the 2D- $CsPtI_3$(DMSO) phase, a large Stokes shift is observed between UV–vis–NIR absorption edge wavelength and PL emission wavelength, due to singlet-to-triplet electron energy transfer via intersystem crossing.[39]

2. Results and Discussion

2.1. 2D Phase Formation

Figure 1a shows the doctor blade process approach with two-step annealing used to synthesize the 2D- $CsPtI_3$(DMSO) phase (refer Supplemental Information for process details). The precursor solution was made in ambient conditions, by fully dissolving CsI and PtI_2 (1:1 mol mol^{-1}) in DMSO solvent at 75 °C with 0.8 M concentration to obtain uniform thickness and compact polycrystalline films, as lower molarity resulted in "coffee-ring" effect (Figure S2, Supporting Information).[40] Pt(II) has been reported to form a complex with DMSO through σ-donation of sulfur lone-pair electrons,[41–44] and the solubility of PtI_2 in DMSO is enhanced with CsI addition (Figure S3b, Supporting Information), indicating the strong interaction between I^- and PtI_2 to form iodoplatinate anions.[45] Therefore, the DMSO-Pt-I-Cs ion cage forms in the precursor colloidal solution according to the "nano-assemble model",[45] as evidenced with the Tyndall effect of the solution (Figure S3c, Supporting Information). The precursor solution appeared dark red, with an absorption edge at

780 nm in the UV–vis absorption spectrum (Figure S4, Supporting Information), attributed to Pt-ligand charge transfer in the ion cage. The wet tacky film doctor bladed onto UV/O_3-treated glass substrate appears yellow, and changes to orange color after a 3 minute anneal at 80 °C. An additional 30 min anneal treatment at 100 °C in vacuum was followed, and no change in the film color observed (see Figure S5, Supporting Information). The UV–vis–NIR absorption edge shows a blue-shift from 780 nm in solution to 600 nm in 2D thin-film phase (Figure S6, Supporting Information). Figure 1b outlines the formation of corner-shared $[PtI_3(DMSO)]^-$ monolayers with Cs^+ ions intercalated in-between for charge neutrality resulting in a 2D- $CsPtI_3(DMSO)$ repeat structure. The sample nomenclature followed in this paper is "Type-temperature of first anneal-temperature of second anneal" example Type-80-100 for 3 minute anneal at 80 °C followed by 30 min anneal at 100 °C.

Figure 2a,b show the SEM micrographs of the 2D-$CsPtI_3(DMSO)$ thin-films, depicting ≈1.3 µm film thickness with 5–10 µm wide columnar grains and few pinholes. EDS analysis (see Figure 2c; Figure S7, Supporting Information) shows Cs:Pt:I:S atomic ratio of 1:1:3:1, confirming stoichiometric $CsPtI_3(DMSO)$, assuming S-element in as-deposited films comes from DMSO (C_2H_6OS) molecules. Figure 2d shows the XRD pattern for the 2D films with a strong diffraction peak at low 2θ of 10.7 degrees, attributed to strong reflection of the planar (001) facet, characteristic of layered perovskites.[16] An interlayer thickness of ≈8.3 Å is estimated from the d-spacing of (001) peak and its harmonic Bragg's reflections, this spacing should be defined by the bonded DMSO molecule and Cs^+ ion. Taken together, the EDS and XRD analyses together indicate a stoichiometric $CsPtI_3(DMSO)$ thin-film that has taken on a 2D structure.

To understand formation of the 2D-phase over that of 0D structures that have been the norm in this material class, it is instructive to consider changes that occur to the sulfur in DMSO as it bonds with the metal-halide. FTIR reveals, for example, an increase of $S^+{\rightarrow}O^-$ bond stretching frequency, ϑ_{SO}, from 1042 cm^{-1} to 1090 cm^{-1} for DMSO by itself and the combined 2D- $CsPtI_3(DMSO)$ films, respectively (see Figure 2e). The increase in energy suggests a strengthening of the $S^+{\rightarrow}O^-$ bond within the DMSO as it reacts with the MHP, which indicates that the 2D-phase is formed via coordination of the sulfur with Pt in the MHP for the reasons outlined subsequently.

DMSO contains two C-S bonds and one dative $S^+{\rightarrow}O^-$ bond along with the lone pair electrons associated with the S- atom (see Figure 2f).[46] This sulfur-based lone pair can interact with the Pt via Pt-S coordination (k-S mode) to form metal complexes. The k-S mode for Pt-S coordination is typically stabilized by synchronous S→Pt σ-donation and Pt→S π-back donation,[42] leading to σ^*- π orbital mixing and spin-orbit coupling.[47] DMSO can also bind with metals via its O atom (k-O mode), as found in complexes like $[Co(DMSO)_6]^+$ and typical DMSO-Lewis-acid-base adducts (e.g., MAI·PbI_2·DMSO).[45,48–51] In this process, the O atom exhibits both σ and π donation because of multiple lone pairs. Both the σ and π donations will decrease electron density of O atom and weaken the $S^+{\rightarrow}O^-$ ionic reaction, resulting in a decrease in the stretching frequency ϑ_{SO}. However, if the DMSO coordinates with the metal atom through the sulfur coordination (k-S mode), for example in Pt(II) and Ru(II), σ donation from S atom (via its one lone pair) to metal and π back donation from metal to S is expected.[42] As a result, there will be a net loss of electron density from S and an increase in its positive charge. Accordingly, the ionic interaction (S^+/O^-) in the S—O bond is strengthened, resulting in increased stretching frequency ϑ_{SO}. Therefore, the observed increase in ϑ_{SO} indicates that DMSO coordinates with transition metal Pt(II) via k-S instead of k-O mode, which is also in line with reported observation on $[PtDMSOCl_3]^-$ and $Pt(DMSO)_2Cl_2$ complexes.[41,43] The observed increase in frequency with k-S mode is also consistent with theory. Calculations predicted that the characteristic ϑ_{SO} stretching vibration band would shift to a high-frequency region by 42 cm^{-1} for DMSO coordinated via the sulfur atom (in $[PtDMSOCl_3]^-$ complex),[43] which agrees with the increase observed in our data (48 cm^{-1}) for formation of 2D- $CsPtI_3(DMSO)$.

Figure 2g shows the absorption spectrum of 2D-$CsPtI_3(DMSO)$ with an absorption edge at 600 nm and a characteristic excitonic peak at 520 nm. The presence of an excitonic peak is further evidence of the 2D perovskite phase, as excitonic binding energies are strong in 2D-layered materials owing to quantum confinement[15,16,52] Figure 2h,i show the Tauc plot for both direct and indirect bandgap analysis resulting in values of 2.21 and 2.05 eV, respectively.

2.2. DFT Calculations for 2D- $CsPtI_3(DMSO)$

DFT calculations were performed to support the phase stability of the 2D-phase and assess the bonding pathways between the DMSO and Pt. All DFT computations were performed using the Vienna ab initio simulation package (VASP),[54] employing projector augmented wave (PAW) pseudopotentials.[55,56] The Generalized Gradient Approximation (GGA)-based PBE[57] +D3 (for empirical van der Waals interactions) functional was used for the $CsPtI_3(DMSO)$ phase, whereas the corrected PBEsol[58] functional was used for the inorganic Cs-Pt-I compounds and reference phases, CsI and PtI_2 or PtI_4. A kinetic energy cut-off of 500 eV was used for the plane wave basis set. Given that all lattice constants for the cubic perovskites and the layered non-cubic phase ranged from ≈9 to ≈11 Å, we used a uniform 4 × 4 × 4 Monkhorst–Pack mesh for sampling the Brillouin zone in all GGA geometry optimization calculations. Atoms were allowed to fully relax to an energy convergence of 10^{-6} eV and a force convergence of −0.03 eV $Å^{-1}$ during the optimization process. The electronic band structure and density of states were calculated using the hybrid HSE06[59] ($\omega = 0.2$ and $\alpha = 0.25$) functional, with static calculations performed on the GGA-optimized geometries. The HSE06-computed bandgap of Cs_2PtI_6 is 1.27 eV, which is slightly underpredicted compared to the experimental value of 1.4 eV.[26,37] The frequency-dependent optical absorption coefficient $I(\omega)$ for the compounds was further calculated from HSE06 as:

$$I(\omega) = \frac{\sqrt{2}\omega}{c}\left(\sqrt{\varepsilon_1(\omega)^2 + \varepsilon_2(\omega)^2} - \varepsilon_1(\omega)\right)^{\frac{1}{2}} \quad (1)$$

from the complex dielectric function $\epsilon(\omega) = \epsilon_1(\omega) + i\epsilon_2(\omega)$, using the LOPTICS tag. The VASP outputs were post-processed using VASPKIT.[60]

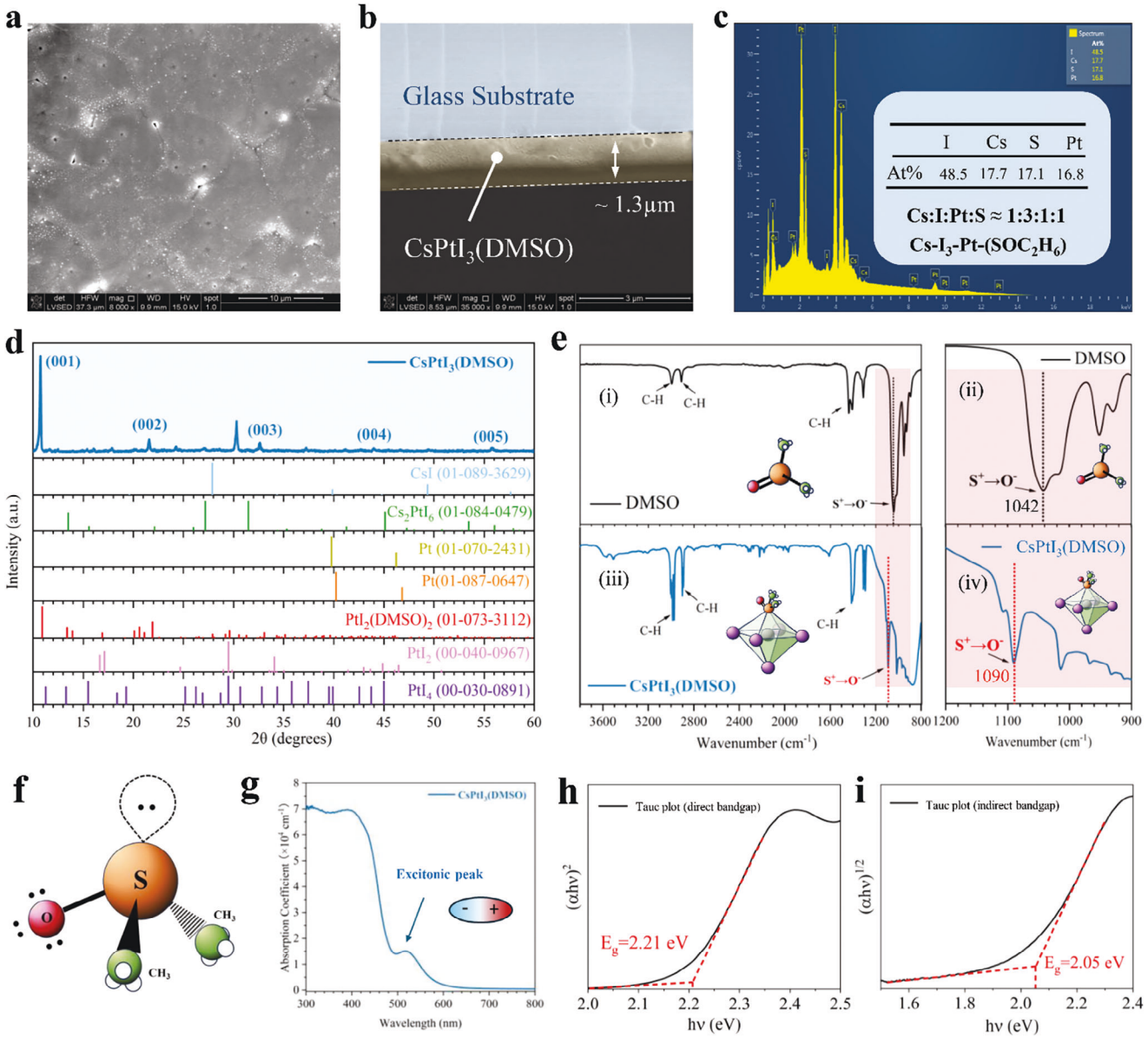

Figure 2. Characterization analysis on the 2D- $CsPtI_3$(DMSO) thin film. a) top-view SEM. b) Cross-section SEM. c) top-view EDX. d) thin film XRD. The resultant thin-film is neither Cs_2PtI_6 or simple mixture/blending of precursor salts/impurities like CsI, PtI_2, or even PtI_4. Instead, a novel and unindexed phase with specific strongest peak at low-diffraction angle 10.7 degrees (2θ), similar to but different from that of DMSO-PtI_2, which should come from the strong reflection of the planar (001) facet of the 2D- $CsPtI_3$(DMSO) and mid-intensity peaks at 21.6, 30.3, and 32.6 degrees (2θ) were formed. The dominant (00l) peaks originated from diffractions between inorganic layers, suggesting high crystallinity and orientation with respect to the substrate e) FTIR spectrum of bare DMSO and $CsPtI_3$(DMSO). For bare DMSO (i and ii), the stretching frequency of $S^+ \rightarrow O^-$ (ϑ_{SO}) appears at 1042 cm^{-1}, while the bands at 1400 and 3000 cm^{-1} are assigned to the CH_3 stretching. ϑ_{SO} of $CsPtI_3$(DMSO) went up (to 1090 cm^{-1}) compared to that of the bare DMSO (1042 cm^{-1}). f) Molecular structure of DMSO. There are three single bonds: two C-S bonds and one dative $S^+ \rightarrow O^-$ bond; and one pair lone electrons associated with the S atom. g) UV–vis absorption spectrum of the $CsPtI_3$(DMSO) thin film featured with the excitonic peak. h) Tauc plot for direct bandgap evaluation. i) Tauc plot for indirect bandgap evaluation. Tauc relation $(\alpha h\nu)^{1/\gamma} = B(h\nu - E_g)$, where $\gamma = 2$ or 1/2 corresponding to indirect and direct transitions, respectively.[53]

The vacancy-ordered Pb-free double perovskite Cs_2PtI_6 crystallizes as a face-centered cubic structure ($Fm\bar{3}m$) with a bandgap of 1.40 eV.[25,36] The PBEsol-relaxed lattice constant of Cs_2PtI_6 is 11.29 Å, which is in good agreement with the previously reported experimental lattice constant of 11.37 Å.[61] We first investigated the effect of gradual addition of Pt interstitials in $Cs_2Pt_xI_6$ (x = 1 for the double perovskite Cs_2PtI_6 and x = 2 for a single perovskite $CsPtI_3$) on the stability, lattice constant, and Pt-I and Cs-I bond lengths; the results of this analysis going from the double perovskite to the single perovskite are presented in **Table 1**. Interestingly, with the addition of Pt, the lattice constant and Cs-I bond length both gradually decreases, whereas the Pt-I bond

Table 1. Lattice parameters, bond lengths, bandgaps (E) and formation energies (ΔE_f) as a function of Pt concentration.

Compound	*a* [Å]	Cs-I [Å]	Pt-I [Å]	$E_{g,HSE}$ [eV]	ΔE^f [eV/atom]
Cs_2PtI_6	11.29	3.99	2.68	1.35	−1.10
$Cs_2Pt_{1.25}I_6$	11.25	3.98	2.73	0.13	−1.09
$Cs_2Pt_{1.50}I_6$	11.15	3.96	2.75	0.12	−1.06
$Cs_2Pt_{1.75}I_6$	11.14	3.94	2.76	0.11	−1.04
$CsPtI_3$	11.10	3.92	2.76	0.00	−0.98

length increases. We calculated the formation energy per atom for any composition as:

$$\Delta E^f\left(Cs_2Pt_xI_6\right) = \frac{E\left(Cs_2Pt_xI_6\right) - 2E\left(Cs\right) - xE\left(Pt\right) - 6E\left(I\right)}{2+x+6} \quad (2)$$

Here, x represents the amount of Pt in one formula unit of the compound, and 2+x+6 is the total number of atoms in the formula unit. The observed reduction in formation energy with increasing concentrations of Pt in Cs_2PtI_6 indicates that the incorporation of Pt destabilizes the perovskite structure. Furthermore, the addition of Pt to the double perovskite also results in eliminating the bandgap.

Next, we focused on simulating a suitable 2D layered $CsPtI_3$(DMSO) structure and comparing its properties with both Cs_2PtI_6 and $CsPtI_3$. Geometry optimization using PBE+D3 showed that the 2D- $CsPtI_3$(DMSO) phase stabilizes with an in-plane lattice parameter of ≈12 Å and an interlayer distance of 8.8 Å, which is in good agreement with the experimental interlayer distance of 8.3 Å. The computed lattice parameters of the 2D-$CsPtI_3$(DMSO) phase are summarized in **Table 2**. The DFT calculated structure also matches the stoichiometric ratio of 1:1:3:1 for Cs:Pt:I:S obtained from EDS analysis. We calculated a decomposition energy for this 2D phase as:

$$\Delta H = E_{CsPtI_3(DMSO)} - E_{CsI} - E_{PtI_2} - E_{DMSO} \quad (3)$$

A negative decomposition energy of ΔH = −1.55 eV per formula unit (p.f.u.) explains the thermodynamic stability of the 2D perovskite complex with respect to its competing phases CsI, PtI_2, and DMSO. The 2D- $CsPtI_3$(DMSO) structure pictured in

Table 2. PBE-D3 computed lattice parameters and HSE06 computed bandgap (E_g) and carrier effective masses (m_h*, m_e*) for the 2D layered $CsPtI_3$(DMSO) phase.

Parameters	DFT value
a(Å)	11.96
b(Å)	9.22
c(Å)	12.20
α (°)	74.52
β (°)	83.64
γ (°)	74.48
E_g (eV)	2.25
m_h*	$-1.21m_0$
m_e*	$+2.01m_0$

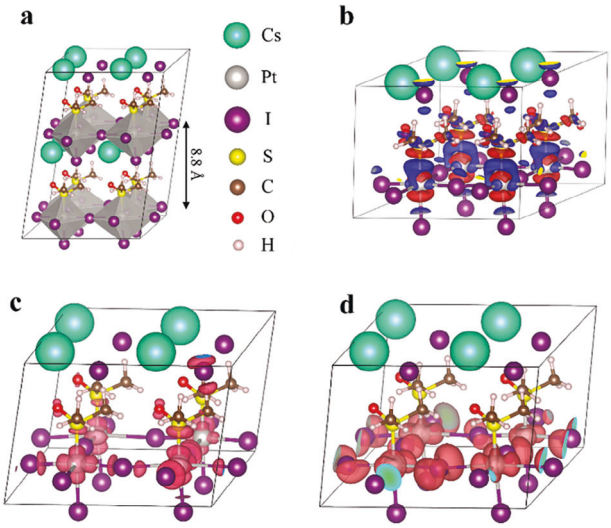

Figure 3. DFT calculated structures: Relaxed geometry of the layered 2D- $CsPtI_3$(DMSO) perovskite structure from PBEsol+D3, showing a) 2 × 1 × 2 supercell. Charge density difference in $CsPtI_3$(DMSO), with red and blue regions representing charge accumulation and depletion respectively, is pictured in b). c,d) show the band decomposed charge density for conduction band (CB) and valence band (VB) respectively.

Figure 3 shows the presence of an S-Pt bond, which corroborates the FTIR experimental findings. The even sharing of electrons between Platinum and Sulfur as observed indicates the formation of a stable σ-bond between Pt and S. Bader charge analysis[62] provides further insights into the S-Pt bond formation mechanism, showing that S has a charge of +1.94 (e^-) whereas Pt is neutral. In $CsPtI_3$, Pt has an oxidation state of 2+ and the donation of lone pair electrons from S to Pt reduces the Pt^{2+} in $CsPtI_3$ to a neutral state, thus forming a σ S-Pt bond. While the decomposition energy ΔH of Cs_2PtI_6 is calculated to be −0.59 eV p.f.u., $CsPtI_3$ (cubic) shows a positive ΔH = 0.19 eV p.f.u., making it thermodynamically unstable with respect to its constituent phases CsI and PtI_2. Thus, it can be concluded that the formation of the covalent Pt-S bond in the 2D- $CsPtI_3$(DMSO) phase helps in stabilizing the single perovskite $CsPtI_3$ in a layered structure as compared to its pristine 3D state.

From HSE06 calculations, the 3D cubic $CsPtI_3$ has a zero bandgap, the vacancy-ordered double perovskite Cs_2PtI_6 has a bandgap of 1.27 eV, and the 2D- $CsPtI_3$(DMSO) phase is found to have a bandgap of 2.25 eV. Thus, we find proof for the bandgap widening from the double perovskite to the layered structure, as seen experimentally. The projected density of states (PDOS) of the 2D- $CsPtI_3$(DMSO) as pictured in **Figure** 4a follows general trends in perovskites with the *Pt-d* and *I-p* orbitals dominating the valence band maximum (VBM) and conduction band minimum (CBM). Figure 4b shows a comparative analysis of the total density of states for $CsPtI_3$, 2D layered $CsPtI_3$(DMSO), and Cs_2PtI_6, revealing how the states shift from one compound to another and how the bandgap changes. DMSO contributes only to the CBM which is corroborated by the band decomposed charge densities shown in Figure 3c,d. The complex also shows high and rising optical absorption coefficient (>10^5 cm^{-1}) as pictured in Figure 4d. The anisotropy observed is characteristic for layered

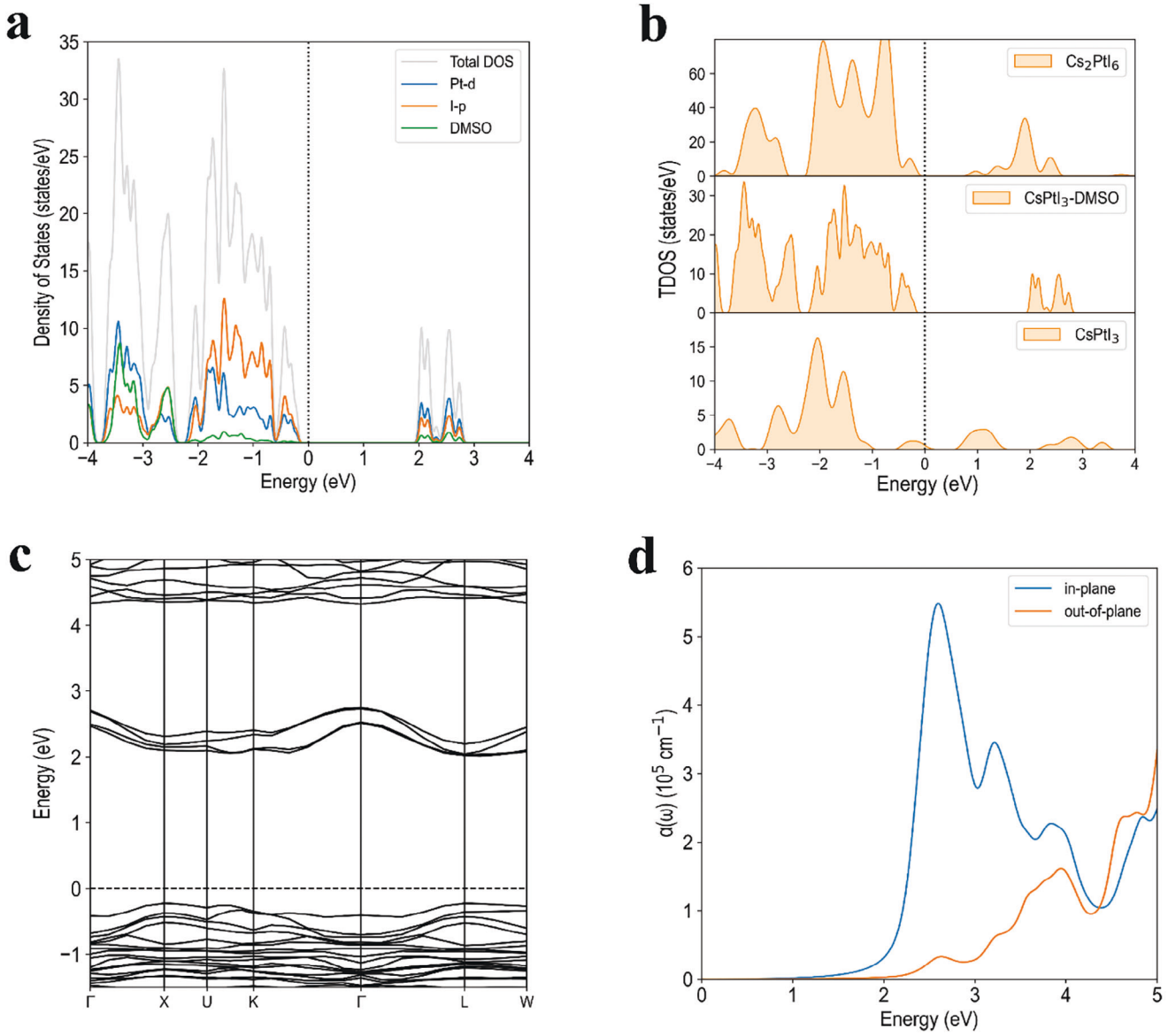

Figure 4. DFT calculated properties of 2D- $CsPtI_3$(DMSO) phase. a) Projected density of states (PDOS) of the 2D layered $CsPt_3$(DMSO). b) Comparison of density of states of $CsPtI_3$, 2D $CsPt_3$(DMSO), and Cs_2PtI_6. c) Band structure of $CsPt_3$(DMSO). d) Optical absorption coefficient as a function of photon energy for 2D layered $CsPt_3$(DMSO).

materials enabling the material to absorb different wavelengths depending on the direction of incident light. Finally, Figure 4c shows the electronic band structure of the complex from HSE06, considering the high symmetry points Γ(0, 0, 0), X(0.5, 0, 0.5), U(0.625, 0.25, 0.625), K(0.375, 0.375, 0.75), L(0.5, 0.5, 0.5), and W(0.5, 0.25, 0.75). The band structure reveals that the bandgap is indirect as opposed to the direct bandgap seen for the double perovskite.

2.3. Intersystem Crossing and Triplet Emission

Figure 5a shows the overlaid steady-state photoluminescence (PL) and UV–vis–NIR absorption spectra of the 2D-$CsPtI_3$(DMSO) phase. Under 532 nm excitation, the PL spectrum shows a weak singlet exciton emission at 610 nm and an intense triplet emission at 852 nm. The weak singlet emission exhibits a small Stokes shift (≈0.03 eV), whereas a large Stokes shift is observed for the triplet emission peak due to intersystem crossing (ISC) and singlet-triplet energy transfer,[47] as has also been reported in 2D halide perovskite $(CH_3NH_3)_2Pb(SCN)_2I_2$.[39] These properties exhibit significant potential in triplet-triplet annihilation (TTA) up-conversion process for photovoltaics and light emitting diodes (LEDs).[39,63–66]

To understand the optical response, the Jablonski diagram in Figure 5b illustrates the overall carrier dynamics in the 2D halide perovskite $CsPtI_3$(DMSO) involving singlet exciton generation, singlet emission (fluorescence), singlet-triplet exciton

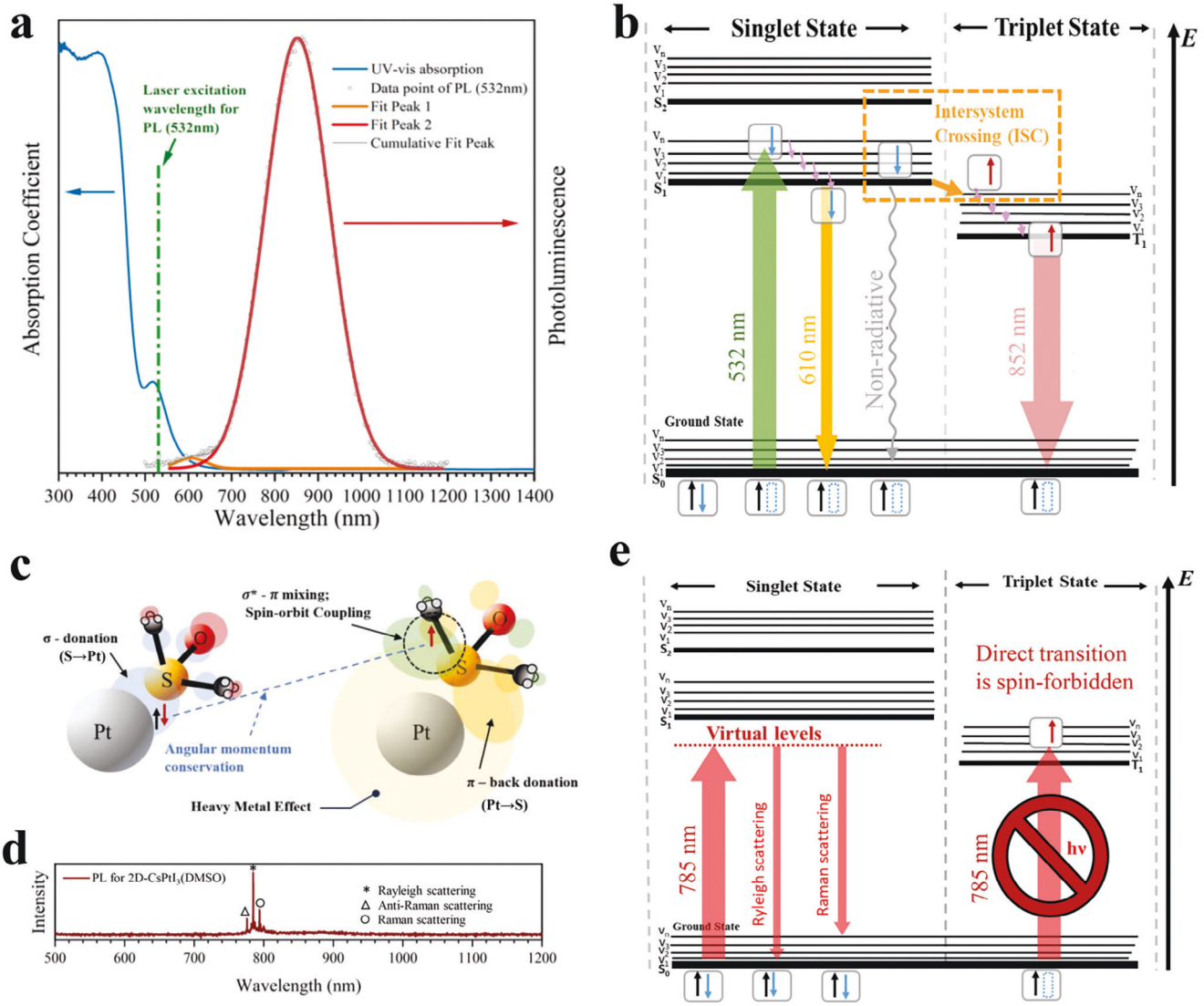

Figure 5. Photoluminescence vs UV–vis absorption and the hypotheses of intersystem crossing and triplet emission. a) The PL spectrum vs UV–vis absorption spectrum of 2D- $CsPtI_3(DMSO)$ thin film. b) Jablonski Diagram involving both singlet florescence and triplet emission via intersystem crossing (ISC), using an excitation wavelength of 532 nm. c) Schematic graphics of the spin-orbit coupling between Pt and DMSO molecules, the intersystem crossing, and the generation of triplet state. d) PL spectrum of 2D- $CsPtI_3(DMSO)$ thin film under excitation of 785 nm laser. e) Schematic illustration for the PL (and Raman) of 2D- $CsPtI_3(DMSO)$ thin film excited with 785 nm laser, in which the generation of a triplet state through direct excitation is a spin-forbidden transition.

energy transfer via intersystem crossing (ISC), and the triplet decay (phosphorescence). Briefly, excitation with 532 nm laser generates singlet excitons (SE), bound electron-hole pairs with opposite spin, through the *1s* exciton transition close to the onset of band edge. The radiative recombination of the singlet excitons results in the singlet emission at 610 nm. However, this process is largely quenched by singlet-triplet exciton energy transfer via ISC, resulting in strong phosphorescence at 852 nm. Intersystem crossing process is facilitated by Pt-S coordination (k-S mode) through interaction of PtI_2 and DMSO molecule (Figure 5c). It is to be noted that UV–vis–NIR absorption spectrum of the 2D- $CsPtI_3(DMSO)$ phase does not exhibit absorption ≈850 nm, supporting the hypothesis singlet-triplet energy transfer process. Additionally, for 785 nm excitation laser, lower energy than the singlet exciton state but higher than the 852 nm emission, no PL emission is observed ≈852 nm. Instead, Raman peaks including Rayleigh scattering, Raman scattering, and anti-Raman scattering were clearly observed in the range of 770–800 nm with 785 nm excitation laser (Figure 5d). This combined evidence supports the hypothesis that 852 nm emission is due to triplet decay to ground state, as the emitting state cannot be directly photoexcited and thus is not a dipole allowed transition,[64] whereas the direct singlet-triplet exciton transition (from ground state to triplet state) is theoretically spin-forbidden (Figure 5e).[67]

Interestingly, 0D- Cs_2PtI_6 phase exhibits a direct bandgap of 1.40 eV,[36] therefore, to confirm 850 nm (1.46 eV) emission is due to ISC or Type-I heterojunction (Figure S8, Supporting

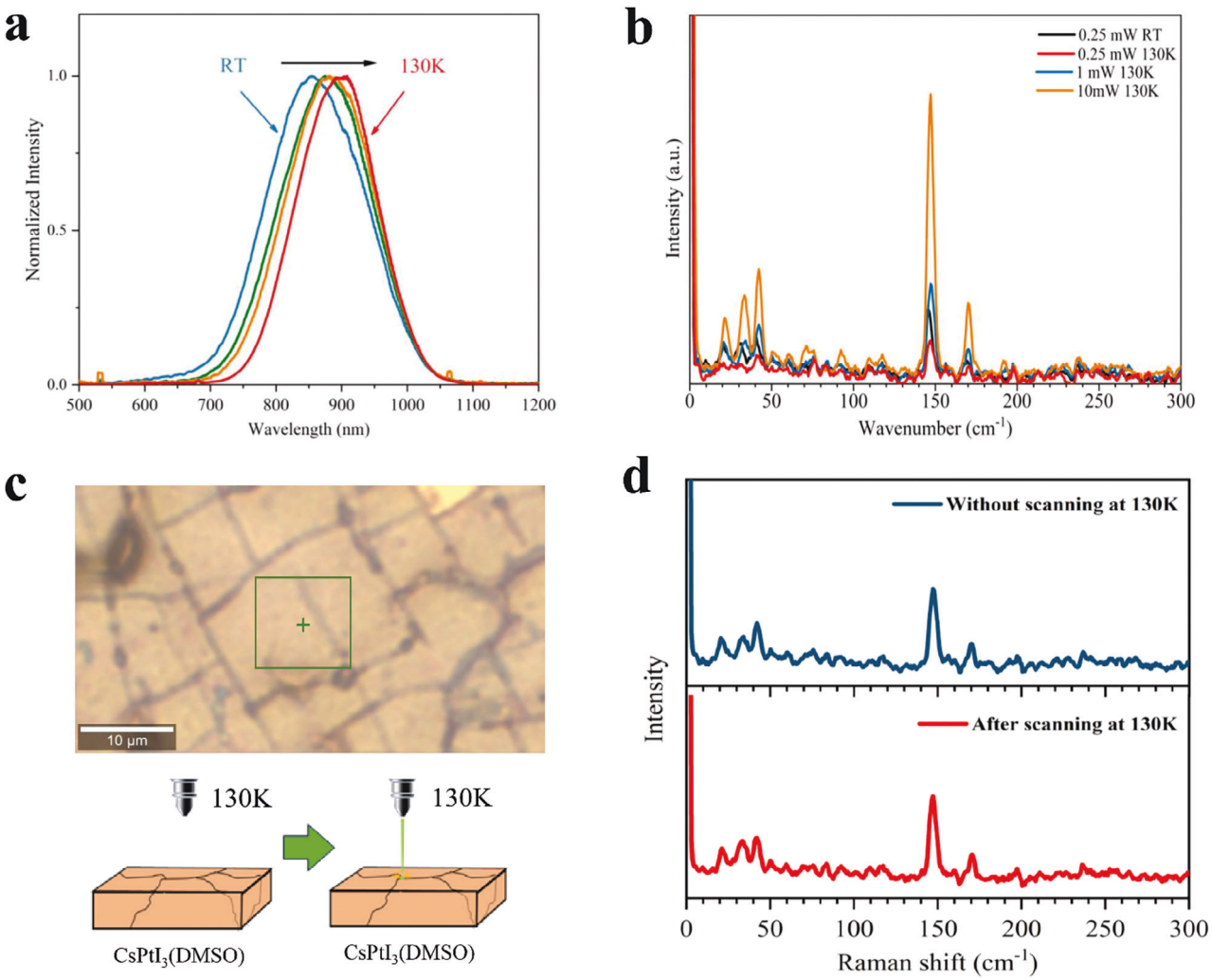

Figure 6. LT-PL of 2D- $CsPtI_3$(DMSO) thin film at 130K. a) PL spectrums of the 2D- $CsPtI_3$(DMSO) during the cooling process. The red-shift of the PL peaks was observed as decreasing the temperature from RT to 130 K. b) The Raman spectrums of the $CsPtI_3$(DMSO) at 130 K with the excitation of 785 nm laser of different power density. c) Photographs and schematic diagrams for the 532 nm laser scanning on 2D- $CsPtI_3$(DMSO) thin film at 130 K. No phase change of the $CsPtI_3$(DMSO) during the laser scanning at 130 K. d) 785 nm Raman spectrums of spot (i) outside and (ii) inside the region of the 532 nm laser scanning at 130 K.

Information), it is important to eliminate thermal effects with low-temperature photoluminescence (LT-PL) measurements. As the temperature decreased, the emission at 610 nm nearly diminished in the "normalized" PL spectrum, and a reversible temperature dependent redshift is observed in the 850 nm peak (**Figure** 6a). The latter peak (850 nm) is dominant in the normalized PL spectrum at decreased temperature. Similar behavior was also reported by Younts et al. studying the singlet-triplet energy transfer in 2D hybrid perovskite $(MA)_2Pb(SCN)_2I_2$.[39] The increased relative intensity ratio of the 850 nm feature over the 610 nm feature at 130 K is due to the higher singlet-triplet transfer efficiency with reduced charge dissociation when thermal energy is removed. And the red-shift of the triplet emission peak can be associated with a modulated superstructure,[39] which begins to appear at lower temperature (see the square lines in Figure 6c) and a return to room temperature alleviates this modulation (Figure S9, Supporting Information). Figure 6b shows Raman spectra obtained at RT and 130 K, where the similarity in response indicates no changes in the structure. Figure 6d shows the Raman spectra after 532 nm laser scan over a square region at 130 K, indicating the 2D phase stability with laser illumination at 130K. More detail about the laser scanning at 130 K is described in Supporting Information (Figure S10, Supporting Information). In essence, our findings demonstrate that the 850 nm emission is due to triplet state decay to ground singlet state and not due to phase transition via Type-I heterojunction formation.

2.4. Stability of 2D- $CsPtI_3$(DMSO)

Existing research on Pt-based halide perovskites has predominantly centered on Cs_2PtX_6, the vacancy-ordered double perovskite, where the Pt element typically assumes a Pt(IV) state,

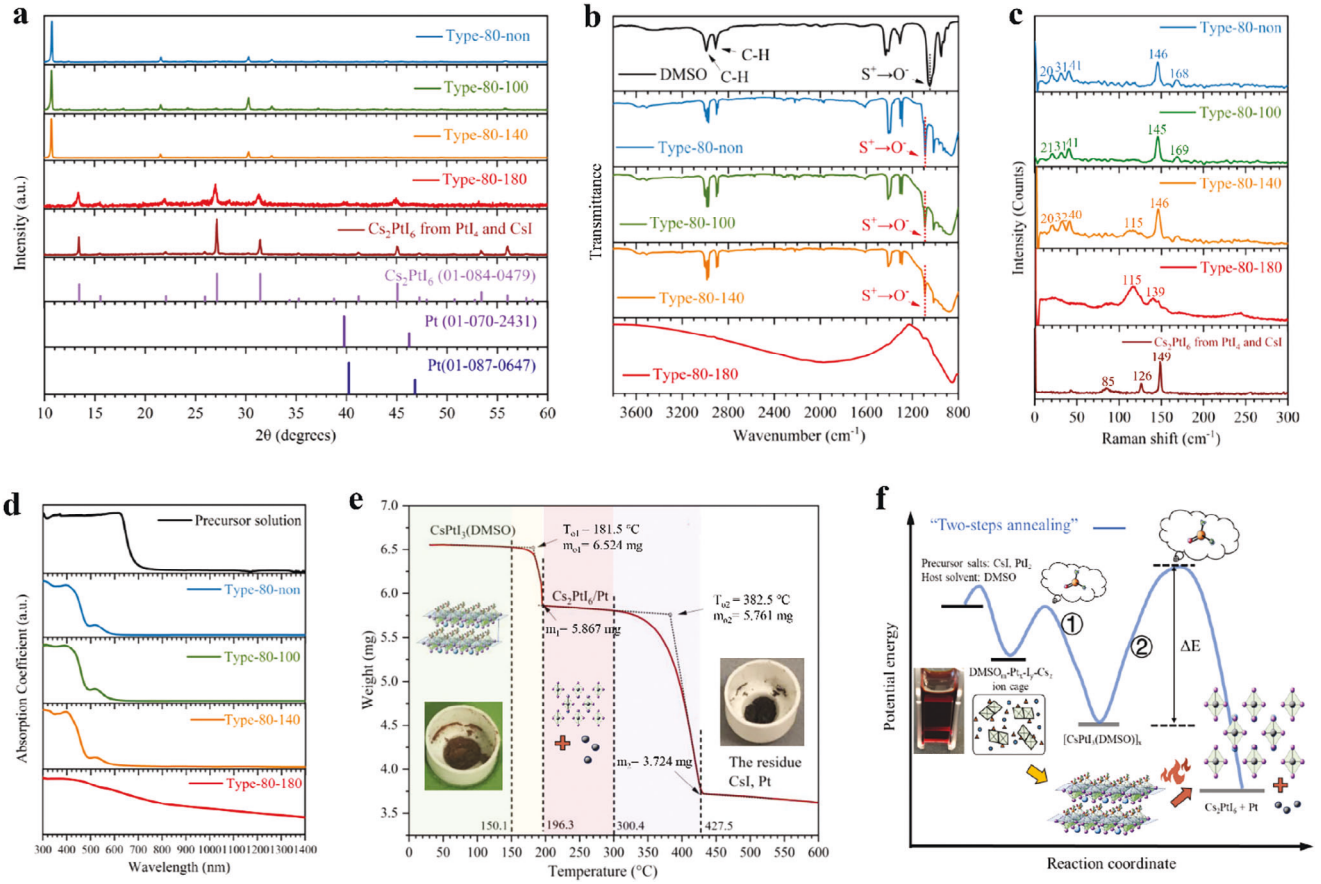

Figure 7. Thermal phase transition during the systematically tuned annealing condition. a) XRD patterns of Type-80-non, Type-80-100, Type-80-140, Type-80-180, and pure Cs_2PtI_6 film prepared from PtI_4 and CsI, respectively. "Type-80-non" indicating the thin film annealed at 80 °C for 3 minutes without a subsequent annealing step, and "Type-80-100" signifying a thin film annealed at 80 °C for 3 min, followed by a 30-minute annealing step at 100 °C. The "Type-80-140" and "Type-80-180" designations indicate similar meanings. b) FTIR spectrum of bare DMSO, Type-80-non, Type-80-100, Type-80-140, and Type-80-180, respectively. c) Raman spectrum of Type-80-non, Type-80-100, Type-80-140, Type-80-180, and pure Cs_2PtI_6 film prepared from PtI_4 and CsI, respectively. d) UV–vis absorption spectrum of precursor solution, Type-80-non, Type-80-100, Type-80-140, and Type-80-180, respectively. Additional UV–vis spectra on annealed films shown in Figure S11 (Supporting Information). e) TGA analysis of the $CsPtI_3$(DMSO) powder over room temperature to 600 °C. f) The reaction coordinate diagram of entire structural transition. SEM micrograph of pure Cs_2PtI_6 and EDS elemental profiling of Type-80-180 thin film is shown in Figures S13 and S14 (Supporting Information) respectively.

due to excellent stability and optoelectronic properties.[22,23] On the other hand, the octahedra factor ($\mu = \frac{R_{Pt}}{R_I}$, $R_{Pt^{2+}} = 80\ pm$, $R_{I^-} = 220\ pm$) of 0.36 and positive decomposition energy for 3D $CsPtI_3$ suggests an unstable perovskite phase. Here, we report a significant breakthrough of successfully synthesizing uniform and stable polycrystalline films with 2D layered $CsPtI_3$(DMSO) phase, where Pt exists in a 2+ state, enabling us to transcend the constraints imposed by lattice limitations and tolerance factors. DMSO plays a dual role here, not only acting as a solvent but also contributing S-lone pair electrons to the formation of the 2D phase. Unlike the frequently observed solvate intermediate phases in solution-processed perovskites, such as MAI·PbI_2·DMSO Lewis-basic-acid adducts,[49,68,69] which undergo rapid decomposition and transformation under mild thermal annealing,[49] the 2D- $CsPtI_3$(DMSO) phase remains stable after undergoing annealing at 100 °C. To further explore the thermal stability of the 2D- $CsPtI_3$(DMSO) phase and distinguish it from metastable intermediate phases, additional thermal and laser annealing, and phase transition results are discussed.

2.4.1. Thermal Stability of the 2D Phase

Figure 7a shows the XRD pattern for 2D- $CsPtI_3$(DMSO) films after 30 min anneals at 100 °C, 140 °C and 180 °C after initial heat treatment at 80 °C to form the 2D-phase (see Figure 1a-ii). XRD after the pre-anneal exhibited the characteristic (001), (002), (003), (004), and (005) peaks of the 2D-phase at 2θ values of 10.7°, 21.6°, 32.6°, 44.0°, and 55.9°, respectively. The XRD pattern and physical color of the films are unchanged after annealing at 100 °C and 140 °C. A change is observed in the Raman spectrum for the 140 °C with the emergence of a peak near 115 cm^{-1} suggesting that some transformation in the film has begun.

Annealing at 180 °C significantly changes the material and indicates it is no longer stable at this temperature. The films

optically blacken and XRD, FTIR, UV–vis–NIR, and Raman responses change considerably (Figure 7a–d). For example, XRD peaks are observed at 2θ values of 13.3°, 15.4°, 21.9°, 27°, 31.3°, 44.9°. These are indexed as (111), (200), (220), (222), (400), and (440) Cs_2PtI_6 planes, respectively (ICSD 37193).[70] The peak at 40° indicates the (111) Pt peak (ICSD 52250).[71] The appearance of these "new" peaks corresponding to Cs_2PtI_6 and Pt is accompanied by a loss of the strong basal peak at 10.7° characteristic of the 2D phase. Spectroscopically, FTIR peaks characteristic of the DMSO molecule in 2D phase (ϑ_{CH} at 1400 cm^{-1} and 3000 cm^{-1} and ϑ_{SO} at 1090 cm^{-1}) nearly disappeared after the high-temperature anneal. The Raman spectrum, meanwhile, exhibits peaks at 115 and 139 cm^{-1} wavenumbers, which is consistent with that observed from Cs_2PtI_6.[72,73] From these results, we conclude that the film transforms 2D- $CsPtI_3$(DMSO) to a 0D mixed phase of Cs_2PtI_6/Pt after the 180 °C anneal.

Thermogravimetric analysis (TGA) in Figure 7e supports this deduction by tracking weight loss as a function of temperature for 2D- $CsPtI_3$(DMSO) films. The result shows a distinct weight loss between 150.1 to 196.3 °C with phase transition onset temperature at 181.5 °C. The weight loss (from m_{01} = 6.524 mg to m_1 = 5.867 mg) matches well with the transformation of 2D halide perovskite $CsPtI_3$(DMSO) to 0D mixed phase Cs_2PtI_6/Pt with the loss of DMSO molecules. Moreover, as the temperature further increases, the 0D Cs_2PtI_6/Pt mixed phase decomposes at 382.5 °C finally resulting in a residue of CsI and Pt according to the weight loss of 35%, summarized in Figure 7f. Figure S12 (Supporting Information) shows the SEM and EDS analysis of films after 180 °C anneal, indicating uniform distribution of Cs, Pt, and I. The 2D phase is stable upto ≈181.5 °C, beyond which it decomposes to a mixture of Cs_2PtI_6 and Pt, the thermal stability being higher than frequently observed solvate intermediate phases (e.g., MAI·PbI_2·DMSO),[49] which is in line with the negative decomposition energy from DFT. Additional effects of annealing are discussed in Supplemental Information (Figures S15–S19, Supporting Information).

2.4.2. Laser Annealing of the 2D Phase

Due to the low thermal conductivity and high absorption coefficient of halide perovskites at 532 nm, the 2D- $CsPtI_3$(DMSO) films are expected to show significant temperature increase during PL measurements, even with laser power as low as 0.1 mW (0.366 mW μm^{-2}) as shown in **Figure 8**a. Figure 8b shows a plot of sample temperature as a function of laser power for film thermal conductivity ranging from 0.1 to 0.5 W m^{-1} K^{-1}, considering thermal conductivity of $CsSnI_3$ and Cs_2PtI_6 as 0.38 W m^{-1} K^{-1} and 0.15 W m^{-1} K^{-1}, respectively.[74,33] During the PL characterization of 2D- $CsPtI_3$(DMSO), we observed changes in the appearance of the thin film (Figure S19, Supporting Information) upon exposure to 532 nm laser illumination, even within a N_2 environment. Additionally, repetitive PL measurements conducted at the same location under N_2 atmosphere resulted in a gradual decrease in the PL emission intensity (Figure S20, Supporting Information), suggesting a bleaching effect. Raman measurements on a 10 µm x 10 µm laser scanned area shows transition of 2D phase to Cs_2PtI_6/Pt mixed phase, with an exposure of 5 sec/spot, as evidenced by the presence of Raman peaks at 117, 138, and

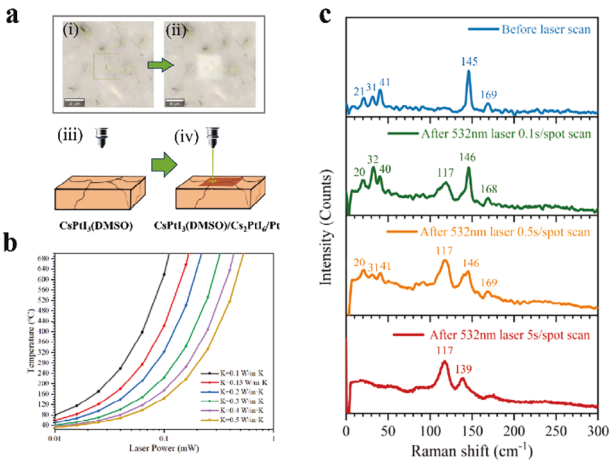

Figure 8. Laser illumination induced phase transition. a) Simulation result diagramed the relation between the highest temperature in beam region and laser power during the PL measurement on perovskite thin films of different thermal conductivity. b) Photographs and Schematic diagrams for the 532 nm laser scanning on 2D- $CsPtI_3$(DMSO) thin film and the regional phase transition of $CsPtI_3$(DMSO) to Cs_2PtI_6/Pt induced. c) 785 nm Raman spectrums of the square centers before and after scanning with different speeds (illumination time) to track the 532 nm laser illumination induced phase change.

172 cm^{-1} wavenumbers as shown in Figure 8c. Notably, no PL emission was observed with 532 nm excitation for the Cs_2PtI_6/Pt mixed phase (Figure S21, Supporting Information). Laser annealing induced phase change is a promising method to make thin film of Pt-doped Cs_2PtI_6, an efficient co-catalyst[75–78] and exceptionally stable perovskite in aqueous solutions with extreme pH values.[22,23]

2.5. Addition of Lewis Bases

The 2D- $CsPtI_3$(DMSO) phase exhibits distinct characteristics compared to typical intermediate phase and Lewis-base-acid complex,[45,48–51] particularly in its higher thermal stability. In typical DMSO-related Lewis-base-acid complexes, DMSO bonds Lewis acid via the k-O mode, while in the 2D- $CsPtI_3$(DMSO), it employs the k-S mode with Pt-S covalent bonding. To investigate the formation mechanism of the 2D phase, we introduced Lewis bases, including acetamide (AA), 1,3-Dimethyl-3,4,5,6-tetrahydro-2(1H)-pyrimidinone (DMPU), and thioacetamide (TAA), into the precursor solution.[79–83] These were added in the same molar ratio of AA/TAA/DMPU: PtI_2: CsI = 1:1:1, and the thin films were doctor-bladed onto glass substrates, followed by two-step annealing (80 °C for 3 minutes and 100 °C for 30 minutes). Detailed experimental procedures can be found in the Supplemental Information.

As seen from molecular structure in **Figure 9**a, AA is anticipated to act as an O-donor.[79] XRD, Raman, FTIR, and UV–vis spectra of samples prepared with AA/DMSO show minimal impact on the formation of 2D- $CsPtI_3$(DMSO) phase. In Figure 9d, the absence of FTIR peak at 1151 cm^{-1}, characteristic to C-N (Figure S22, Supporting Information), suggests no AA-related complexes formed, despite its stronger Lewis basicity.[82] Additionally, similar UV–vis absorption edges in AA/DMSO and pure

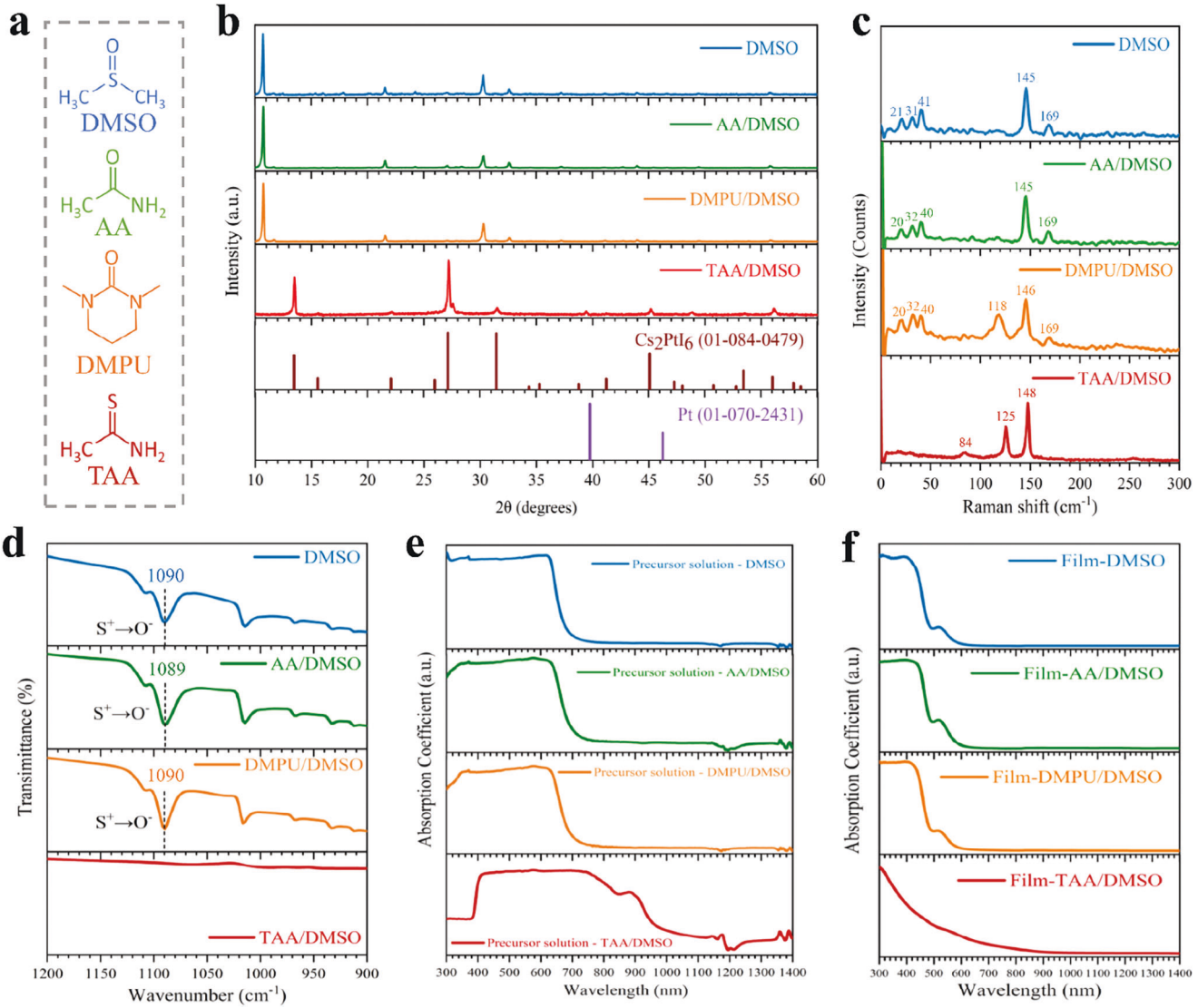

Figure 9. a) Molecular structures of DMSO, AA, DMPU, and TAA, respectively. b) XRD pattern of Film-DMSO, Film-AA/DMSO, Film-DMPU/DMSO, and Film-TAA/DMSO, respectively. c) Raman spectrum of Film-DMSO, Film-AA/DMSO, Film-DMPU/DMSO, and Film-TAA/DMSO, respectively. d) FTIR spectrum of film Film-DMSO, Film-AA/DMSO, Film-DMPU/DMSO, and Film-TAA/DMSO, respectively. e) UV–vis spectrum of precursor solution contain solvent of DMSO, AA/DMSO, DMPU/DMSO, and TAA/DMSO, respectively. f) UV–vis spectrum of film Film-DMSO, Film-AA/DMSO, Film-DMPU/DMSO, and Film-TAA/DMSO, respectively.

DMSO precursor solutions indicate minimal influence on the ion cage formation, indicating the preference for S-Pt over O-Pt bonding.

DMPU, an O-donor, with a higher donor number of 33 compared to DMSO of 29.8,[83] acts as a stronger Lewis base due to its additional nitrogen (N) atoms. XRD analysis (Figure 9b) of films made with DMPU/DMSO precursor solution reveals a dominant 2D phase, with a discernible peak at 118 cm^{-1} observed in Raman spectrum (Figure 9c), hinting at a small fraction of Cs_2PtI_6/Pt. Additionally, C═O FTIR peak at 1637 cm^{-1} in DMPU shifts to 1608 cm^{-1} suggesting Pt co-ordination with S may be retarded in the presence of DMPU (Figure S23, Supporting Information).[84] The characteristic S═O FTIR peak at 1090 cm^{-1} (Figure 9d) is observed in both AA/DMSO and DMPU/DMSO precursor solutions indicating minimal influence on ion-cage with the two additives, and similarity in the UV–vis spectra of precursor solution (Figure 9e) and films (Figure 9f) support this interpretation. These findings suggest that while a fraction of DMPU-related Lewis-base-acid complex competes with the 2D phase, but the latter remains more stable.

The addition of TAA,[79–81] a S-donor, into the precursor solution, significantly impedes the formation of the 2D-$CsPtI_3$(DMSO) phase, as evidenced by XRD pattern, showing the formation of crystalline Cs_2PtI_6 and Pt. Further, Raman spectra on films prepared with TAA/DMSO precursor solution show sharp peaks associated with Cs_2PtI_6 and minimal shift or broadening. The UV–vis spectrum of the TAA/DMSO precursor solution exhibited a noticeable red-shift in the absorption edge

compared to pure DMSO precursor solution, likely due to formation of Cs_2PtI_6 in the precursor solution. A red-shifted absorption edge was also observed compared to films prepared with only DMSO-based precursor solutions. These observations suggest that presence of TAA results in changes in the Pt-S coordination in DMSO and retards the formation of the 2D phase. Competitive coordination between DMSO-Pt and TAA-Pt via Pt-S coordination hinders the formation of DMSO-Pt-I-Cs ion cages and the 2D phase, leading directly to formation of mixed Cs_2PtI_6 and Pt. The introduction of stronger Lewis bases clearly shows the distinct role of Pt-S bonding in the formation of 2D- $CsPtI_3$(DMSO) phase, which differs from conventional Lewis-base-acid interactions where DMSO typically coordinates with metals via oxygen (O). A competitive Pt-S co-ordination of TAA molecule retards the formation of 2D phase and results in the formation of mixed Cs_2PtI_6 and Pt.

3. Conclusion

In conclusion, our investigation has revealed the novel organic-inorganic hybrid 2D layered $CsPtI_3$(DMSO) phase, showcasing promising optoelectronic properties, stabilized by the donation of S-lone pair electrons from DMSO solvent. The thermal stability of this phase is notable, up to 181.5 °C, beyond which it undergoes a phase transition to a mixture of Cs_2PtI_6 and Pt. The interaction between Pt(II) and DMSO, characterized by both σ-donation of electrons from S-to-Pt and π-back donation, plays a crucial role in stabilizing the layered structure of 2D- $CsPtI_3$(DMSO), as confirmed by negative decomposition energy through DFT calculations. This Pt-S interaction induces spin-orbit coupling, facilitating intersystem crossing (ISC) and singlet-to-triplet energy transfer of excitons, resulting in a large Stokes shift. Singlet emission peak at 610 nm and triplet emission peak at 850 nm are observed using photoluminescence spectroscopy. Furthermore, our findings highlight the influence of strong S-donors like TAA in disrupting the formation of the 2D layered structure, leading to the formation of Cs_2PtI_6 and Pt instead. Exploration and optimization of these materials hold promise for addressing critical societal challenges and fostering a sustainable energy future.

Supporting Information

Supporting Information is available from the Wiley Online Library or from the author.

Acknowledgements

This work was supported by the National Science Foundation CAREER Award No. 2046944.

Conflict of Interest

The authors declare no conflict of interest.

Data Availability Statement

The data that support the findings of this study are available from the corresponding author upon reasonable request.

Keywords

2D metal halide perovskites, intersystem crossing, lone pair electrons, Stokes shift, transition metal

Received: September 8, 2024
Revised: October 5, 2024
Published online:

[1] X. Li, Y. Wu, S. Zhang, B. Cai, Y. Gu, J. Song, H. Zeng, *Adv. Funct. Mater.* **2016**, *26*, 2435.
[2] R. E. Brandt, J. R. Poindexter, P. Gorai, R. C. Kurchin, R. L. Z. Hoye, L. Nienhaus, M. W. B. Wilson, J. A. Polizzotti, R. Sereika, R. Žaltauskas, L. C. Lee, J. L. Macmanus-Driscoll, M. Bawendi, V. Stevanović, T. Buonassisi, *Chem. Mater.* **2017**, *29*, 4667.
[3] A. Dey, J. Ye, A. De, E. Debroye, S. K. Ha, E. Bladt, A. S. Kshirsagar, Z. Wang, J. Yin, Y. Wang, L. N. Quan, F. Yan, M. Gao, X. Li, J. Shamsi, T. Debnath, M. Cao, M. A. Scheel, S. Kumar, J. A. Steele, M. Gerhard, L. Chouhan, K. Xu, X. Wu, Y. Li, Y. Zhang, A. Dutta, C. Han, I. Vincon, A. L. Rogach, et al., *ACS Nano* **2021**, *15*, 10775.
[4] C. Liu, Y.-B. Cheng, Z. Ge, *Chem. Soc. Rev.* **2020**, *49*, 1653.
[5] A. S. Marques, R. M. Faria, J. N. Freitas, A. F. Nogueira, *Ind. Eng. Chem. Res.* **2021**, *60*, 7145.
[6] J. Ye, M. M. Byranvand, C. O. Martínez, R. L. Z. Hoye, M. Saliba, L. Polavarapu, *Angew. Chem., Int. Ed.* **2021**, *60*, 21636.
[7] H. Liu, S. Bansal, *Mater Today Energy* **2023**, *32*, 101230.
[8] S. Pan, J. Li, Z. Wen, R. Lu, Q. Zhang, H. Jin, L. Zhang, Y. Chen, S. Wang, *Adv. Energy Mater.* **2022**, *12*, 2004002.
[9] L. Clinckemalie, D. Valli, M. B. J. Roeffaers, J. Hofkens, B. Pradhan, E. Debroye, *ACS Energy Lett.* **2021**, *6*, 1290.
[10] T. A. Chowdhury, M. A. Bin Zafar, M. Sajjad-Ul Islam, M. Shahinuzzaman, M. A. Islam, M. U. Khandaker, *RSC Adv.* **2023**, *13*, 1787.
[11] P. Wu, S. Wang, X. Li, F. Zhang, *Matter* **2022**, *5*, 1137.
[12] J. Li, H. L. Cao, W. Bin Jiao, Q. Wang, M. Wei, I. Cantone, J. Lü, A. Abate, *Nat. Commun.* **2020**, *11*, 310.
[13] M. S. Collin, S. K. Venkatraman, N. Vijayakumar, V. Kanimozhi, S. M. Arbaaz, R. G. S. Stacey, J. Anusha, R. Choudhary, V. Lvov, G. I. Tovar, F. Senatov, S. Koppala, S. Swamiappan, *J. Hazardous Mater. Adv.* **2022**, *7*, 100094.
[14] Q. Wali, F. J. Iftikhar, M. E. Khan, A. Ullah, Y. Iqbal, R. Jose, *Org. Electron.* **2020**, *78*, 105590.
[15] R. L. Z. Hoye, J. Hidalgo, R. A. Jagt, J. Correa-Baena, T. Fix, J. L. MacManus-Driscoll, *Adv. Energy Mater.* **2022**, *12*, 2100499.
[16] L. Mao, C. C. Stoumpos, M. G. Kanatzidis, *J. Am. Chem. Soc.* **2019**, *141*, 1171.
[17] L. Etgar, *Energy Environ. Sci.* **2018**, *11*, 234.
[18] M. Daub, H. Hillebrecht, *Angew. Chem., Int. Ed.* **2015**, *54*, 11016.
[19] J. Li, C. C. Stoumpos, G. G. Trimarchi, I. Chung, L. Mao, M. Chen, M. R. Wasielewski, L. Wang, M. G. Kanatzidis, *Chem. Mater.* **2018**, *30*, 4847.
[20] J. Li, Q. Yu, Y. He, C. C. Stoumpos, G. Niu, G. G. Trimarchi, H. Guo, G. Dong, D. Wang, L. Wang, M. G. Kanatzidis, *J. Am. Chem. Soc.* **2018**, *140*, 11085.
[21] Z.-K. Chen, W. Ye, H.-Z. Lin, C. Yu, J.-H. He, J.-M. Lu, *ACS Sens.* **2021**, *6*, 3800.
[22] M. Hamdan, M. Manoj, J. S. Halpati, A. K. Chandiran, *Sol. RRL* **2022**, *6*, 2101092.
[23] M. Hamdan, A. K. Chandiran, *Angew. Chem., Int. Ed.* **2020**, *59*, 16033.
[24] J. P. Jayaraman, M. Hamdan, M. Velpula, N. S. Kaisare, A. K. Chandiran, *ACS Appl. Mater. Interfaces* **2021**, *13*, 16267.

[25] S. Yang, L. Wang, S. Zhao, A. Liu, Y. Zhou, Q. Han, F. Yu, L. Gao, C. Zhang, T. Ma, *ACS Appl. Mater. Interfaces* **2020**, *12*, 44700.
[26] H. Peng, L. Xu, Y. Sheng, W. Sun, Y. Yang, H. Deng, W. Chen, J. Liu, *Small* **2021**, *17*, 2102149.
[27] S. Suzuki, M. Tsuyama, *Opt. Mater.* **2021**, *119*, 111323.
[28] P. Bhumla, M. Jain, S. Sheoran, S. Bhattacharya, *J. Phys. Chem. Lett.* **2022**, *13*, 11655.
[29] H. H. AbdElAziz, M. Taha, W. M. A. El Rouby, M. H. Khedr, L. Saad, *Heliyon* **2022**, *8*, e10808.
[30] A. Amjad, S. Qamar, C. Zhao, K. Fatima, M. Sultan, Z. Akhter, *RSC Adv.* **2023**, *13*, 23211.
[31] T. Tang, X. Diao, Y. Tang, *Chem. Phys. Lett.* **2023**, *826*, 140678.
[32] S. Yang, Q. Han, L. Wang, Y. Zhou, F. Yu, C. Li, X. Cai, L. Gao, C. Zhang, T. Ma, *Chem. Eng. J.* **2021**, *426*, 131838.
[33] M. Sajjad, Q. Mahmood, N. Singh, J. A. Larsson, *ACS Appl. Energy Mater.* **2020**, *3*, 11293.
[34] X. Ye, A. Liu, Y. Zhao, Q. Han, T. Kitamura, T. Ma, *Int. J. Energy Res.* **2022**, *46*, 8471.
[35] X. Ye, A. Liu, L. Gao, C. Zhang, L. Yan, S. Wen, T. Ma, *EcoMat* **2023**, *5*, 131838.
[36] D. Schwartz, R. Murshed, H. Larson, B. Usprung, S. Soltanmohamad, R. Pandey, E. S. Barnard, A. Rockett, T. Hartmann, I. E. Castelli, S. Bansal, *Physica Status Solidi – Rapid Research Letters* **2020**, *14*, 2000182.
[37] S. Shinde, M. Hamdan, P. Bhalla, A. K. Chandiran, *ACS Eng. Au* **2024**, *4*, 224.
[38] National Renewable Energy Laboratory. Best Research-Cell Efficiency Chart, Photovoltaic Research, NREL, https://www.nrel.gov/pv/interactive-cell-efficiency.html (accessed: July 2024).
[39] R. Younts, H. Duan, B. Gautam, B. Saparov, J. Liu, C. Mongin, F. N. Castellano, D. B. Mitzi, K. Gundogdu, *Adv. Mater.* **2017**, *29*, 1604278.
[40] Y. Deng, Q. Wang, Y. Yuan, J. Huang, *Mater. Horiz.* **2015**, *2*, 578.
[41] A. A. A. AL-Dulaimy, Master Thesis, AL-Nahrain University, **2002**.
[42] N. S. Panina, M. Calligaris, *Inorganica Chim Acta* **2002**, *334*, 165.
[43] K. Panina, *Russ. J. Inorg. Chem.* **1998**, *43*, 81.
[44] K. Panina, *Russ. J. Inorg. Chem.* **1999**, *44*, 738.
[45] Q. Hu, L. Zhao, J. Wu, K. Gao, D. Luo, Y. Jiang, Z. Zhang, C. Zhu, E. Schaible, A. Hexemer, C. Wang, Y. Liu, W. Zhang, M. Grätzel, F. Liu, T. P. Russell, R. Zhu, Q. Gong, *Nat. Commun.* **2017**, *8*, 15688.
[46] T. Clark, J. S. Murray, P. Lane, P. Politzer, *J. Mol. Model* **2008**, *14*, 689.
[47] D. Beljonne, Z. Shuai, G. Pourtois, J. L. Bredas, *J. Phys. Chem. A* **2001**, *105*, 3899.
[48] J.-W. Lee, Z. Dai, C. Lee, H. M. Lee, T.-H. Han, N. De Marco, O. Lin, C. S. Choi, B. Dunn, J. Koh, D. Di Carlo, J. H. Ko, H. D. Maynard, Y. Yang, *J. Am. Chem. Soc.* **2018**, *140*, 6317.
[49] N. Ahn, D.-Y. Son, I.-H. Jang, S. M. Kang, M. Choi, N.-G. Park, *J. Am. Chem. Soc.* **2015**, *137*, 8696.
[50] R. Szostak, A. de Souza Gonçalves, J. N. de Freitas, P. E. Marchezi, F. L. de Araújo, H. C. N. Tolentino, M. F. Toney, F. das Chagas Marques, A. F. Nogueira, *Chem. Rev.* **2023**, *123*, 3160.
[51] L. C. Chen, C. H. Tien, Y. C. Jhou, W. C. Lin, *Energies* **2020**, *13*, 2438.
[52] Z. Xiao, W. Meng, B. Saparov, H.-S. Duan, C. Wang, C. Feng, W. Liao, W. Ke, D. Zhao, J. Wang, D. B. Mitzi, Y. Yan, *J. Phys. Chem. Lett.* **2016**, *7*, 1213.
[53] F. A. Mir, *Results Phys.* **2014**, *4*, 103.
[54] G. Kresse, J. Furthmüller, *Phys. Rev. B* **1996**, *54*, 11169.
[55] G. Kresse, D. Joubert, *Phys. Rev. B* **1999**, *59*, 1758.
[56] G. Kresse, J. Hafner, *J. Phys.: Condens. Matter* **1994**, *6*, 8245.
[57] J. P. Perdew, K. Burke, M. Ernzerhof, *Phys. Rev. Lett.* **1996**, *77*, 3865.
[58] J. P. Perdew, A. Ruzsinszky, G. I. Csonka, O. A. Vydrov, G. E. Scuseria, L. A. Constantin, X. Zhou, K. Burke, *Phys. Rev. Lett.* **2008**, *100*, 136406.
[59] J. Heyd, G. E. Scuseria, M. Ernzerhof, *J. Chem. Phys.* **2003**, *118*, 8207.
[60] V. Wang, N. Xu, J.-C. Liu, G. Tang, W.-T. Geng, *Comput. Phys. Commun.* **2021**, *267*, 108033.
[61] C. Airoldi, D. C. Bradley, H. Chudzynska, M. B. Hursthouse, K. M. A. Malik, P. R. Raithby, *Chem. Informationsdienst* **1981**, *12*, https://doi.org/10.1002/chin.198101083.
[62] R. F. W. Bader, *Atoms in Molecules: A Quantum Theory*, Clarendon Press, Oxford Science Publications, Oxford, England **1990**.
[63] H. Hu, D. Zhao, Y. Gao, X. Qiao, T. Salim, B. Chen, E. E. M. Chia, A. C. Grimsdale, Y. M. Lam, *Chem. Mater.* **2019**, *31*, 2597.
[64] J. T. Dubose, P. V. Kamat, *Chem. Rev.* **2022**, *122*, 12475.
[65] K. Mase, K. Okumura, N. Yanai, N. Kimizuka, *Chem. Commun.* **2017**, *53*, 8261.
[66] A. Chemmangat, J. Chakkamalayath, J. T. DuBose, P. V. Kamat, *J. Am. Chem. Soc.* **2024**, *146*, 3352.
[67] D. F. Evans, *Proc. R. Soc. Lond. A* **1960**, *255*, 55.
[68] J.-W. Lee, S.-H. Bae, Y.-T. Hsieh, N. De Marco, M. Wang, P. Sun, Y. Yang, *Chem* **2017**, *3*, 290.
[69] J. Jiao, C. Yang, Z. Wang, C. Yan, C. Fang, *Results Eng.* **2023**, *18*, 101158.
[70] G. Thiele, C. Mrozek, D. Kammerer, K. Wittmann, *Z. Naturforsch. B* **1983**, *38*, 905.
[71] E. A. Owen, E. L. Yate, *Lond. Edinb. Dublin Philos. Mag. J. Sci.* **1933**, *15*, 472
[72] S. F. Parker, K. P. J. Williams, T. Smith, A. J. Ramirez-Cuesta, L. L. Daemen, *Inorg. Chem.* **2022**, *61*, 5844.
[73] W. Baechle, H. W. Rotter, G. Thiele, R. J. H. Clark, *Inorganica Chim Acta* **1992**, *191*, 121.
[74] W. Lee, H. Li, A. B. Wong, D. Zhang, M. Lai, Y. Yu, Q. Kong, E. Lin, J. J. Urban, J. C. Grossman, P. Yang, *Proc. Natl. Acad. Sci. USA* **2017**, *114*, 8693.
[75] P. Zhou, H. Chen, Y. Chao, Q. Zhang, W. Zhang, F. Lv, L. Gu, Q. Zhao, N. Wang, J. Wang, S. Guo, *Nat. Commun.* **2021**, *12*, 4412.
[76] X. Guo, J. Li, Y. Wang, Z. Rui, *Catal. Today* **2022**, *402*, 210.
[77] Y. Wu, Q. Wu, Q. Zhang, Z. Lou, K. Liu, Y. Ma, Z. Wang, Z. Zheng, H. Cheng, Y. Liu, Y. Dai, B. Huang, P. Wang, *Energy Environ. Sci.* **2022**, *15*, 1271.
[78] S. Wang, A. Lu, C.-J. Zhong, *Nano Converg.* **2021**, *8*, 4.
[79] L. Yu, T. Guo, H. Yuan, Z. Zhang, Z. Deng, R. Zhao, M. Zheng, J. Zhang, W. Xu, X. Liu, Z. Hu, Y. Zhu, *Chem. Eng. J.* **2021**, *420*, 129931.
[80] J. W. Lee, H. S. Kim, N. G. Park, *Acc. Chem. Res.* **2016**, *49*, 311.
[81] I. Wharf, T. Gramstad, R. Makhija, M. Onyszchuk, *Can. J. Chem.* **1976**, *54*, 3430.
[82] NIST Chemistry WebBook, NIST Standard Reference Database Number 69, "Infrared Spectrum of Acetamide" Data compiled by NIST Mass Soecctromtery Data Center 2018 (accessed: February 2024).
[83] F. Cataldo, *Eur. Chem. Bull.* **2015**, *4*, 92.
[84] Spectral Database for Organic Compounds SDBS, SDBS No. 23266, "Infrared Spectra of 1,3-Dimethyl-3,4,5,6-Tetrahydro-2(1H)-Pyrimidinone", by National Institute of Advanced Industrial Science and Technology. https://Sdbs.Db.Aist.Go.Jp (accessed: May 2024).